Research Article

Fabrication of UV Photodetectors Based on Photoelectrochemically Etched Nanoporous Silicon: Effect of Etchants Ratio

Asad A. Thahe [iD],[1] **Motahher A. Qaeed** [iD],[2] **Suhail Najm Abdullah,**[3]
Ibrahim M. Badawy [iD],[4] **Hasan Alqaraghuli** [iD],[5] **Yasser Saleh Mustafa Alajerami** [iD],[6]
A. Mindil [iD],[2] **and Ammar AL-Farga** [iD][7]

[1]*Department of Medical Physics, College of Applied Science, University of Fallujah, Baghdad, Iraq*
[2]*Faculty of Science, University of Jeddah, Jeddah, Saudi Arabia*
[3]*Department of Medical Equipment Technology Engineering, Al-Rasheed University College, Baghdad, Iraq*
[4]*Energy Materials Laboratory, School of Sciences and Engineering, The American University in Cairo, New Cairo 11835, Egypt*
[5]*Faculty of Electrical Engineering, Mechatronics and Automatic Control Department, University of Technology Malaysia, Johor Bahru 81310, Malaysia*
[6]*Faculty of Applied Medical Sciences, Medical Imaging Department, Al-Azhar University-Gaza, Gaza, State of Palestine*
[7]*Faculty of Science, Department of Biochemistry, University of Jeddah, Jeddah, Saudi Arabia*

Correspondence should be addressed to Asad A. Thahe; asaad.thahe@yahoo.com

Despite several attempts to enhance the electrical and charge carrier transport characteristics of porous silicon (PSi), the requisite conditions for optimally synthesizing n-PSi with appealing optoelectronic properties are yet to be achieved. Therefore, this research explores the effect of the chemical ratio of precursor materials ($HF:C_2H_6O:H_2O_2$) on the surface morphology, crystalline structure, and optical and electric properties of PSi. The PSi was produced by photoelectrochemical etching followed by anodization of the n-type Si under light illumination. The properties of the as-prepared PSi were studied by means of microscopic and spectroscopic techniques. The $HF:C_2H_6O:H_2O_2$ chemical ratio was optimized at $2:1:1$. A metal–semiconductor–metal (MSM) ultraviolet photodetector (Pt/n-PSi/Pt) was fabricated, which exhibited high performances under UV light (365 nm) illumination. The photodetector was shown to be highly stable and reliable with a rapid rise time of 0.56 s at a bias voltage of +5 V. The MSM photodetector displayed responsivity (R_p) of 9.17 A/m at 365 nm, which significantly exceeds the values reported for TiC/porous Si/Si in some contemporary research. The photodetector fabricated from n-PSi, synthesized at an optimum chemical ratio ($2:1:1$) exhibited the best photo-detection performance, possibly due to the high porosity and defect-free state of the n-PSi thin films.

1. Introduction

Porous silicon (PSi) has shown great potential, particularly in the manufacture of light-emitting diodes (LEDs), on account of its visible light emission at room temperature. The very large and reactive internal surface of the PSi layer makes it characteristically different from its bulk counterpart. Thus, the internal surface of the PSi layer plays a vital role in determining its intrinsic properties [1]. The simple and cost-effective fabrication associated with its good optical properties further increases its potential application in integrated optics

and photonics [2]. As a result, several attempts have been made to enhance the electrical and charge carrier mobility attributes of PSi [3]. Nonetheless, the optimal settings for synthesizing n-PSi with the sought-after optoelectronic properties are yet to be attained. For instance, n-PSi is presently being investigated as a precursor material for the manufacture of ultraviolet photodetectors (UVPDs) because of its high visibility and UV photoluminescence under ambient conditions [4]. Given such demand, this study is carried out to optimize the electrical and optical attributes of n-PSi as input

material for the manufacture of metal–semiconductor–metal (MSM) UVPDs.

Specifically, this paper examines the effect of the chemical ratio of precursor materials (HF:C_2H_6O:H_2O_2) on the structural and optoelectronic properties of PSi. The duration of photoelectrochemical etching, applied voltage or current, and illumination intensity on the properties of the synthesized n-PSi were also explored. In addition, the photoresponse of MSM UVPDs fabricated from different PSi layers (synthesized at different chemical ratios) in the dark and under illumination was also studied.

2. Experimental Details

Before the photoelectrochemical etching for the growth of n-PSi, single crystalline wafers of n-type Si (111) with a thickness range of 205–306 μm were cut into squares of 1.5 cm^2, which were then cleaned using the Radio Corporation of America (RCA) technique. An anodization cell was fabricated from Teflon. The Si wafer was affixed and sealed through an O-ring, while its front side was subjected to electrolyte mix solution of hydrogen fluoride (HF) solution (48%), ethanol (C_2H_6O, 99.9%), and hydrogen peroxide (H_2O_2).

2.1. Preparation of Porous Si (PSi). The first step involves the immersion of the Si wafer into the electrolyte mix solution of HF, ethanol, and H_2O_2. Pure H_2O_2 was included to eliminate the H_2 gas bubbles at the sample surface that were produced in the course of anodization [5]. The Si wafer and a platinum wire were utilized as the anode and cathode, respectively. The PSi layer was synthesized inside the HF solution (HF: C_2H_6O:H_2O_2 = 2 : 1 : 1) using the DC process at a fixed current density of 45 mA/cm^2 and an etching duration of 30 min under external incandescent light. The HF, ethanol (C_2H_6O), and H_2O_2 were mixed at different ratios (1 : 1 : 0, 1 : 3 : 0, and 2 : 1 : 1). The as-prepared PSi layers were then utilized to fabricate MSM-UVPD. To ensure the formation of a Schottky contact (resulting from its higher work function), $a \approx 150$ nm thick platinum (Pt) layer was placed over the PSi surface. The MSM-UVPD structure comprises two interdigitated Schottky contacts (electrodes with five fingers) with a length of ≈3.3 mm, a width of 30 μm, and a spacing of 400 μm, as shown in Figure 1. The electron beam evaporation technique was employed to deposit the metal finger mask by means of the ATO 306 vacuum coater.

2.2. Morphological and Optical Characterizations. The structure of the as-prepared PSi was determined via X-ray diffraction using the PANalytical X'PertPro Diffractometer equipped with Cu–K radiation (wavelength 1.54056 Å) and operated at 40 kV and 30 mA. The surface morphology of the as-obtained PSi layer was analyzed using a high-resolution field emission scanning electron microscope (FESEM NOVA NANO SEM 450). Photoluminescence (PL) spectra of the samples were recorded using Jobin Yvon HR 800 UV spectrophotometer equipped with a He–Cd laser with a wavelength, λ, of 325 nm at 20 mW. Current–voltage (I–V) and current–time (I–t) plots of the fabricated MSM-UVPD were recorded using the Keithley electrometer (model 6517 A).
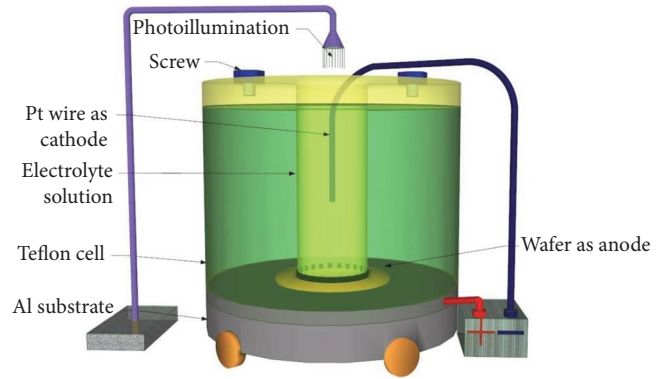

FIGURE 1: The experimental set-up used for the photoelectrochemical etching of Si.

3. Results and Discussion

3.1. Morphological Observations. The porosity (P) of the synthesized PSi layer was calculated using Equation (1).

$$P(\%) = \frac{M1 - M2}{M1 - M3}, \tag{1}$$

where M_1 and M_2 represent the weight of the sample pre- and postanodization, respectively, while M_3 denotes the weight of the sample following removal of the PSi layer using 3% KOH for 60 s [5]. The porosity is ~70.33%. The thickness of the porous layer (d) was calculated to be 4.07 nm using Equation (2) [6]:

$$d = \frac{(m1 - m3)}{(D \times A)}. \tag{2}$$

The FESEM micrographs of the n-PSi samples for different chemical ratios (1 : 1 : 0, 1 : 3 : 0, and 2 : 1 : 1) are shown in Figure 2. The dark and bright regions denote the nucleation of Si nanocrystallites and intergranular pores, respectively. Here, the crystallinity of Si structure declines, thereby increasing the density of the pores. Thus, it can be interpreted that the pore size and density of n-PSi nanostructures can be modified by regulating the chemical ratio of HF: C_2H_6O:H_2O_2 in solution. Figure 3 depicts the FESEM cross-sectional features of n-PSi prepared under different chemical ratios (HF:C_2H_6O:H_2O_2). The thickness of the layer varies significantly with the chemical ratio, with values of 22.11, 32.60, and 40.75 μm for 1 : 1 : 0, 1 : 3 : 0, and 2 : 1 : 1, respectively.

3.2. Surface Topography Characterization using AFM. It is imperative to emphasize that the AFM method provides images of the surface of pores, which makes it disadvantageous compared with the SEM technique [7]. Nonetheless, this technique can be performed using minute magnitude of forces [8]. The AFM image of PSi grown onto n-type Si (Figure 4) shows the usual rough surface morphology of
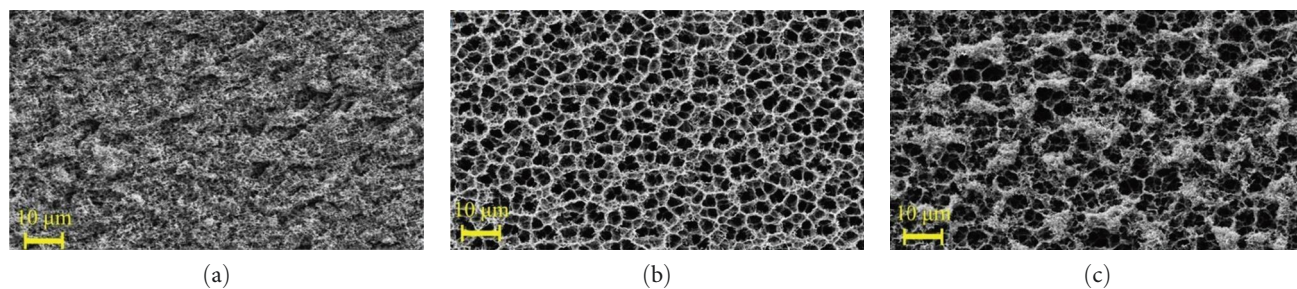
(a)

(b)

(c)

Figure 2: FESEM top-view images of the synthesized n-PSi upon chemical ratio (HF:C$_2$H$_6$O:H$_2$O$_2$): (a) (1:1:0), (b) (1:3:0), and (c) (2:1:1).

H 1 = 22.11 μm

H 1 = 32.60 μm

H 1 = 40.75 μm

(a)

(b)

(c)
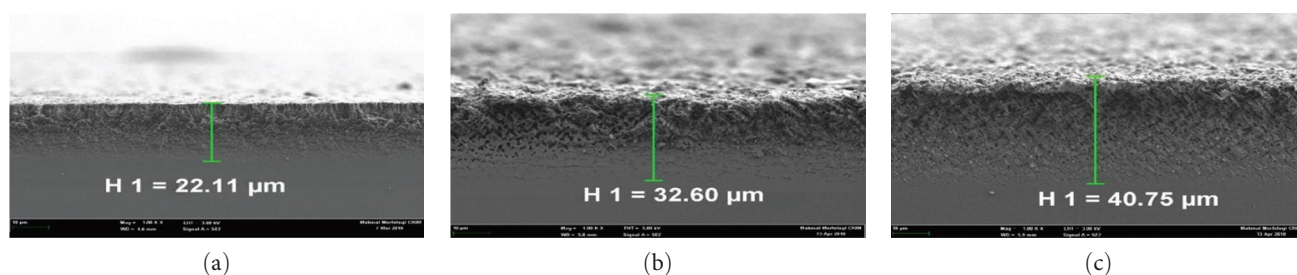
Figure 3: FESEM cross-section images of n-PSi at different chemical ratios (HF:C$_2$H$_6$O:H$_2$O$_2$): (a) (1:1:0), (b) (1:3:0), and (c) (2:1:1).

(a)

(b)

(c)
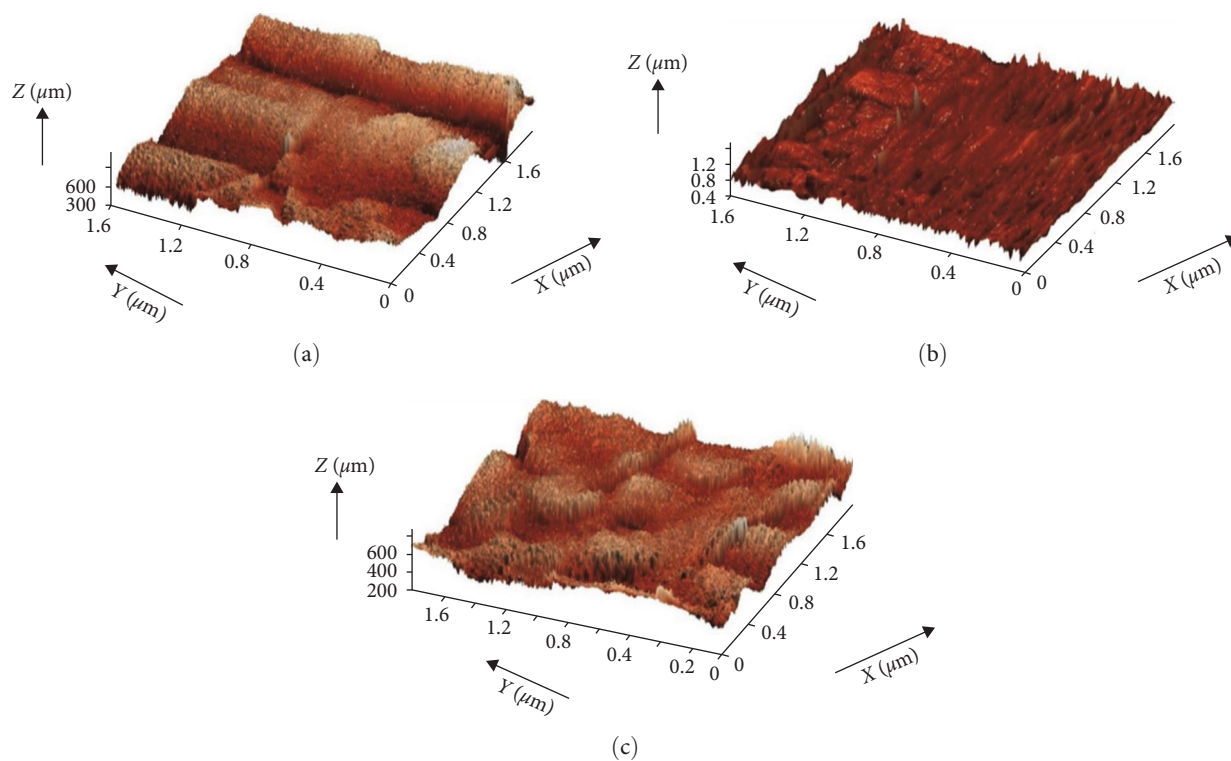
Figure 4: 3D AFM images of the n-PSi samples for different chemical ratios (HF:C$_2$H$_6$O:H$_2$O$_2$): (a) (1:1:0), (b) (1:3:0), and (c) (2:1:1).

the nanostructure. The 3D AFM image of the as-anodized PSi layer grown onto n-type for etching duration of 30 min at 45 mA cm^{-2} shows that the n-PSi film is uniform with many columnar-shaped grains. The scanned area film of 5 μm × 5 μm appears smooth with a root mean square (RMS) of ∼47.5 nm for roughness.

3.3. Structural Analysis. The XRD spectra of the PSi layers were obtained over 2θ range of 25°–30° (Figure 5). The relatively high intensity and broad peak centered at ∼28.42° can be indexed as (111) reflection of the Si cubic structure, which is consistent with JCPDS card no. 00-041-1426. No effect of the chemical ratio is noticeable. The increase in lattice

FIGURE 5: XRD patterns of n-type crystalline Si (111) wafer and the grown PSi layers at different chemical ratios (HF:C₂H₆O:H₂O₂).

constant in PSi silicon is observed, which can be attributed to an increase in induced stress by the formation of a native oxide on the pore surface.

The crystallite size (D) was derived using Scherrer's equation as presented in Equation (3) [9]:

$$D = \frac{0.9\lambda}{B \cos \theta},$$ (3)

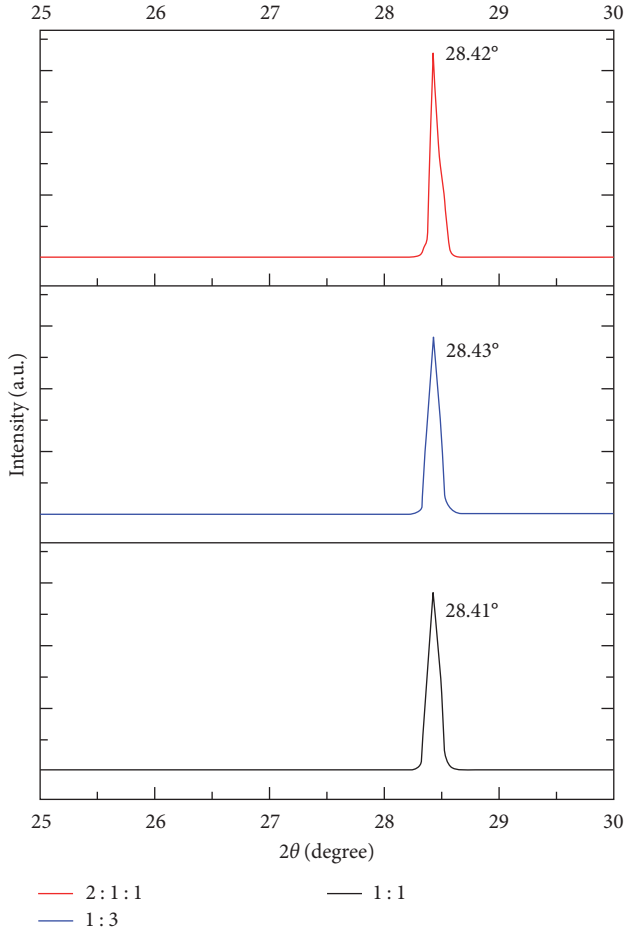where λ (= 1.5406 Å), B, and θ symbolize the incident X-ray wavelength, full-width half maximum (FWHM), and Bragg's angle of diffraction, respectively. The crystallite size increases with higher ethanol concentration from 10.87 nm for $1:1:0$ to 14.38 nm for $1:3:0$, but slightly increases to 14.51 nm with the addition of hydrogen peroxide at the expense of ethanol ($2:1:1$).

The strain (ε_{zz}) in the direction of the (111) diffraction plane of n-PSi was calculated using the basic equation expressed below (Equation 4):

$$\varepsilon_{zz} = \frac{C - C_0}{C_0} \times 100,$$ (4)

where C and C_0 represent the experimental lattice constants of PSi and bulk Si from the JCPDS card (≈ 0.542 nm),

TABLE 1: Variation of (111) peak position, FWHM, crystallite size, and strain as a function of chemical ratio (HF:C₂H₆O:H₂O₂).

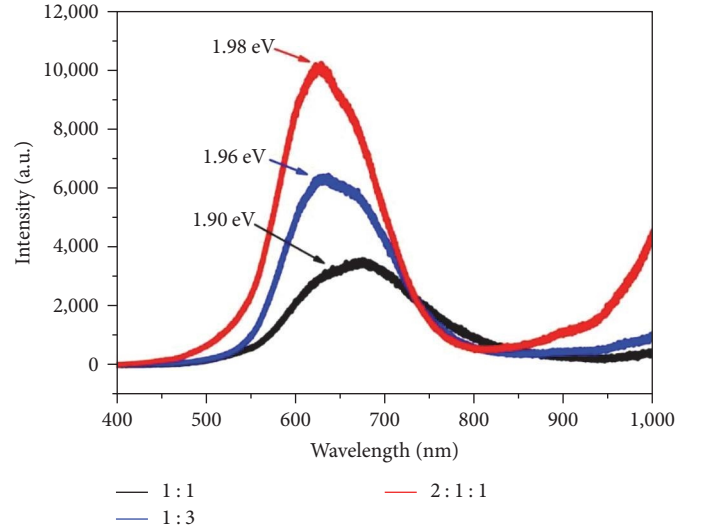| Chemical ratio (HF:C₂H₆O:H₂O₂)	2θ (°)	FWHM (°)	Crystallite size (nm)	Strain (%)
(1:1:0)	28.4477	0.7872	10.87	0.0136
(1:3:0)	28.4444	0.5904	14.38	0.0103
(2:1:1)	28.4576	0.5904	14.51	0.0102

FIGURE 6: PL spectra of synthesized PSi at different chemical ratios (HF:C₂H₆O:H₂O₂).

TABLE 2: The energy band gap and wavelength (nm) of the grown n-PSi at different chemical ratios (HF:C₂H₆O:H₂O₂).

Chemical ratio (HF:C₂H₆O:H₂O₂)	Energy band gap (eV)	Wavelength (nm)
(1:1:0)	1.90	650.80
(1:3:0)	1.96	631.71
(2:1:1)	1.98	624.96

respectively. It can be observed from Table 1 that the chemical ratio affects the strain, where it decreases with increasing ethanol concentration and decreased further with the addition of hydrogen peroxide. Furthermore, the positive value of (ε_{zz}) indicates tensile character.

3.4. Photoluminescence Spectroscopy. The PL emission spectra of PSi synthesized at different chemical ratios (HF:C₂H₆O:H₂O₂) under room temperature are shown in Figure 6. A well-defined and distinct peak is discernible around 624.96 nm. As the concentration of ethanol and hydrogen peroxide were increased, this prominent emission peak made a blue shift, the width reduced and the intensity increased, suggesting the influence of the chemical ratio. The observed blue shift can be related to the quantum confinement effect [9, 10]. The reduction in particle (grains) size due to the variation in HF:C₂H₆O:H₂O₂ chemical ratio (from $1:1:0$ to $1:3:0$) may account for the strong quantum size confinement that explains the increases in energy band gap [11, 12] (see Table 2). Afterward, the simple
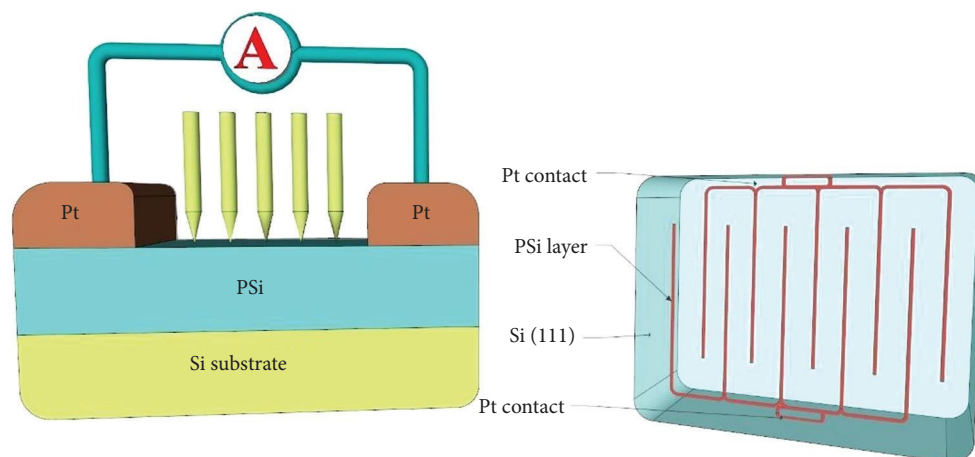
FIGURE 7: Graphic representation of the MSM (Pt/n-PSi/Pt) photodetector fabricated based on photoelectrochemically etched n-PSi layer.

photoelectrochemical technique for the preparation of PSi nanostructures presents different properties, indicating enhanced thermal stability, thus confirming their applicability as thermal insulators [13].

3.5. Fabrication of MSM Photodetector. Figure 7 presents a schematic illustration of the MSM photodetector (Pt/n-PSi/Pt) fabricated in this study. The Pt grid comprises two interdigital contacts (electrodes), which consist of five fingers each. The dimensions of each finger, in terms of width, spacing, and length are $\approx 230\,\mu m$, $\approx 400\,\mu m$, and 3.3 mm, respectively, with an active area of about 0.25 cm^2. The Schottky contacts (Pt/n-PSi) are determined based on PSi electron affinity and Pt work function. Given the electron affinity of the semiconductor and the nature of metal, the junction exhibits a Schottky behavior [14], where the charge carriers are mobilized unrestrained, into or outside the semiconductor [15]. In this case, minimum resistance is observed as the contact is traversed. Since the n-PSi is an n-type semiconductor, the work function value of the used metal is proximate or less compared to its electron affinity [16]. The theoretical work function value of n-PSi (111) is 2.06 eV, which is considerably dependent on concentration of O$_2$ vacancies produced in the synthesis process [17], whereas that of Pt is 4.08 eV [18]. The rectifying properties of the MSM photodetector are confirmed by the development of a Schottky barrier at the Pt–Si junction, which indicates its efficiency as a diode.

3.6. Electrical Characterization of the MSM Photodetector. I–V curves of the Pt/n-PSi/Pt UV photodetector were obtained for different experimental conditions that include dark UV light illumination (365 nm/1.5 mW cm^{-2}), and bias voltage range of +5 V to −5 V. Figure 8 displays the Schottky I–V property under both forward and reverse bias conditions at +5 V. The Schottky contact was detectable at the interface linking the Pt electrodes to n-PSi nanostructure. The measurement of current both in the dark and under illumination involves placing the photodetector in a black box to prevent incident light in the measurements. At a bias voltage of +5 V, the dark current $(1.81 \times 10^{-6}\,A)$ is lower than values in related

contemporary research [19]. In this context, it is imperative to emphasize that the signal-to-noise (S/N) ratio of the detector is strongly dependent on the low dark current [20]. The measured high photocurrent of $109 \times 10^{-6}\,A$ under UV illumination can be ascribed to the large surface area-to-volume ratio and improved crystal structure of the synthesized n-PSi nanostructures. In addition, the use of higher etching/anodization current density remarkably improved the I–V response of the MSM UV photodetector. Moreover, the conversion of the optical signal to an electrical signal via the inflow of charges inside the circuit indicates the successful completion of the photodetector. This implies that the I–V properties of the MSM photodetector are dependent on the anodization current density.

The novel structural arrangement of the MSM photodetector, i.e., two Schottky contacts linked end-to-end, oriented positively toward the variation of reverse/forward bias voltage from −5 to +5 V, as it is recognized that sensitivity is improved as the bias voltage is increased. In addition, at higher bias voltage, n-PSi can absorb light intensely to produce additional e^{-}–h^{+} pairs inside the space charge area. Therefore, the production of an electric field inside the space charge region, which results in the partition of the charge carriers, is dependent on the applied high bias voltage, thus generating an increasing rise in thermionic emission to enhance the mobility of the carriers. Accordingly, there is an exponential rise in current with the applied voltage, which surpasses the potential barrier. The bias voltage provides adequate energy to the electrons to disrupt the barrier height and generate a strong diffusion current [21], resulting in the shift of holes/electrons in the direction of positive/negative terminals, which accounts for the generation of photocurrent in the exterior contact.

The results showed that the sample prepared at HF: C$_2$H$_6$O:H$_2$O$_2$ chemical ratio, current density, and etching duration of 2 : 1 : 1, 45 mA cm^{-2}, and 30 min, respectively, exhibited a very high photocurrent, possibly due to the considerable resistivity and Schottky barrier height. The sample prepared at 1 : 1 : 0 displayed the highest dark current, which can be attributed to other carrier transport mechanisms.
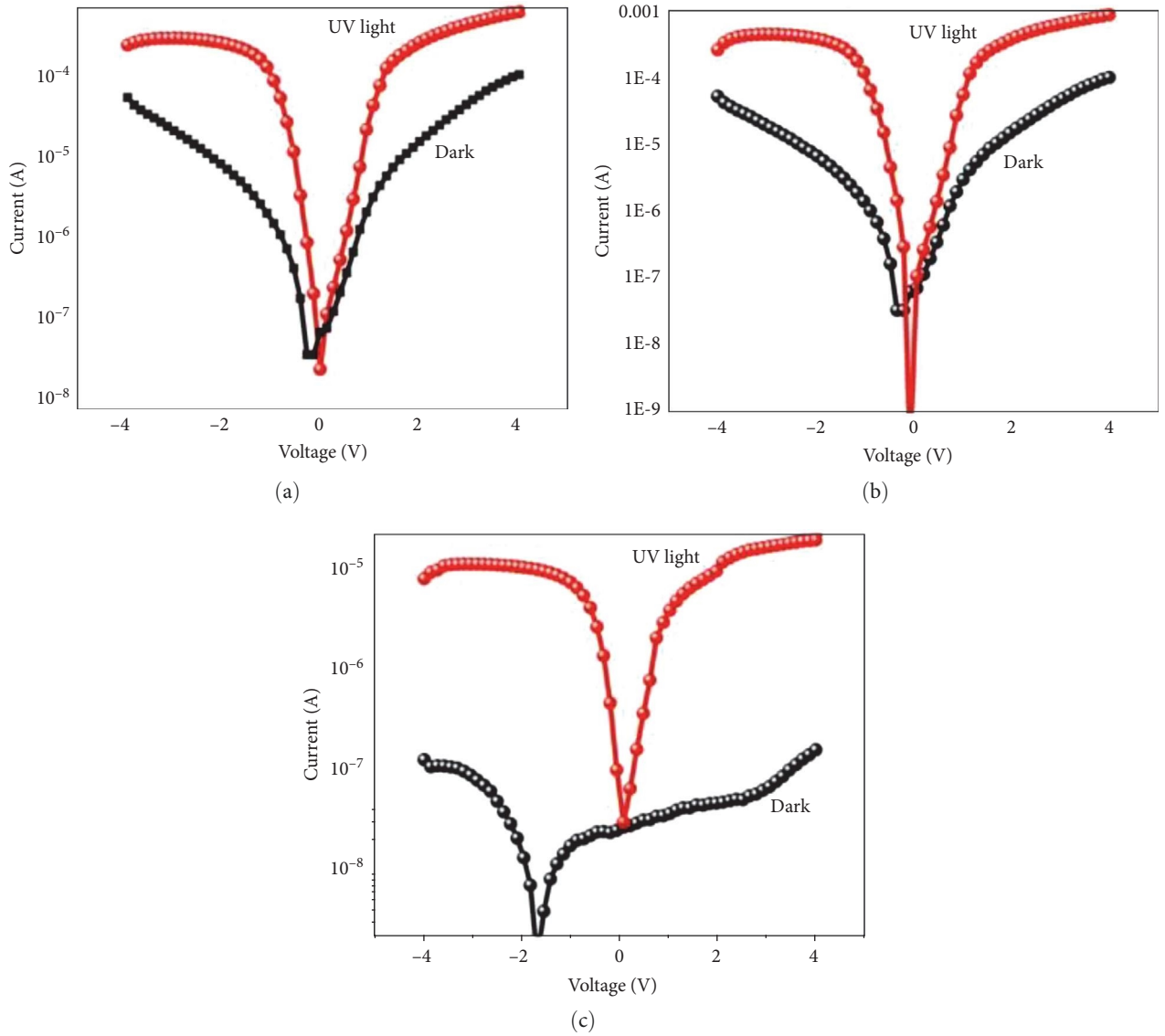
(a)

(b)

(c)

FIGURE 8: I–V properties of the Pt/n-PSi/Pt photodetector in dark and under UV illumination for different (HF:C_2H_6O:H_2O_2) ratios: (a) (1:1:0), (b) (1:3:0), and (c) (2:1:1).

For instance, by disregarding the thermionic emission over the Schottky barrier, the transport of charges can be ensured through the mechanism of direct tunneling of carriers [22]. At chemical ratio of 2:1:1, the dark/leakage current is lowest, indicating improved electrical properties at this ratio. It also suggests the influence of hydrogen peroxide in enhancing photocurrent detection. Thus, photodetection using MSM can be achieved with optical transparency in the UV region, which is consistent with an earlier study by Hadjersi and Gabouze [23]. The ideality factor and Schottky barrier height certainly confirm the efficiency of the fabricated photodetector.

This study further evaluated the effect of chemical ratio on UV photodetection (under UV light illumination at wavelength of 365 nm) at +3, +5, and +7 V bias voltages that are applied at an interval of 20 s (Figure 9). It is observed that the fabricated photodetector exhibits exceptional repeatability and stability at the selected bias voltages (+3, +5, and +7 V) with a rectangular-shaped I–t curve for each on/off cycle. The recovery and rise times of the photodetector were calculated from the I–t curves. It is discernible that the recovery and rise times are very swift for the different bias voltages. Regardless of the anodization current density, the spectral sensitivity was observed to be optimum at an applied bias voltage of +5 V. Afterwards, evaluating the photoresponse behavior of the detectors was maintained at a bias voltage of 5 V, while the HF:C_2H_6O:H_2O_2 ratio was varied. Thus, the spectral responsivity values of the three photodetectors (derived from different HF:C_2H_6O:H_2O_2 ratios) were evaluated at +5 V. After the application of thermionic emission–diffusion [21], the Schottky barrier height (Φ_B) and ideality factor (n) values were determined using the underlying equations (Equations 5 and 6):

$$I = I_0 \exp\left(\frac{qV}{nkT}\right)\left[1 - \exp\frac{-qV}{kT}\right], \tag{5}$$
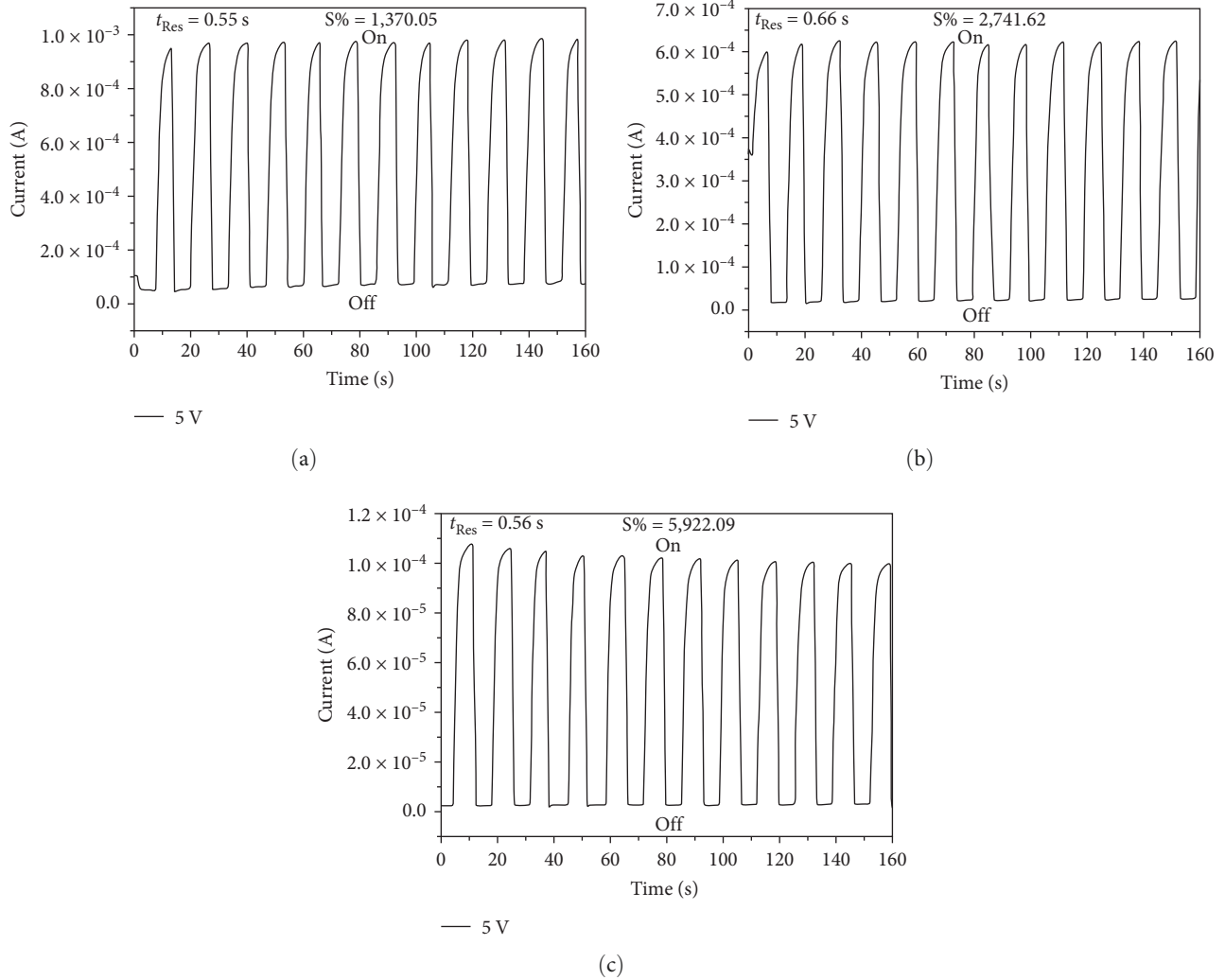
(a)

(b)

(c)

FIGURE 9: Bias voltage-dependent photoresponse (under UV light illumination) of the photodetector fabricated from n-PSi grown at different chemical ratios (HF:C_2H_6O:H_2O_2): (a) (1:1:0), (b) (1:3:0), and (c) (2:1:1).

$$I_0 = AR^*T^2\exp\left[\frac{-\Phi_B}{kT}\right], \tag{6}$$

where I_0, T, k, R^*, A, and q denote saturation anodization current, temperature, Boltzmann constant, effective Richardson coefficient ($\approx 112\,A\,cm^{-2}\,K^2$), area of the Schottky contact ($\approx 0.25\,cm^2$), and electronic charge. The intercept of the ln I–V plot was utilized to determine the Φ_B value. A slight variation in Φ_B was observed with varying chemical ratios. This is attributed to differential modification of the surface roughness of PSi, which significantly affects the n-PSi/Pt interface [24]. The average Φ_B value of 0.96 eV was derived for n-PSi photodetector fabricated at the optimum HF: C_2H_6O:H_2O_2 chemical ratio of 2:1:1 at a bias voltage of +5 V. The high porosity achieved at large anodization chemical ratio accounts for the rise in Φ_B, resulting in a shift in Fermi level toward the valence band, thereby reducing the dark current. The obtained high ideality factor values are consistent with the higher density of interfacial states [25]. The observed enhancement can also be attributed to the presence of two heterojunctions, substrate–PSi interface and n-PSi–Pt boundary [26]. Moreover, the presence of a heterogeneous barrier height can lead to a higher increase in n compared to the values reported in contemporary studies [27].

Furthermore, the I–t curve was utilized for the calculation of sensitivity (S) of the photodetector at a bias voltage of +5 V using the underlying relation (Equation 7) [10]:

$$S(\%) = \frac{I_{ph} - I_d}{I_d} \times 100, \tag{7}$$

where I_{ph} denotes photocurrent, and I_d represents the dark current density. The stability and repeatability of the photocurrent values of MSM photodetectors are ascertained during each on/off phase. The response and recovery times for the chemical ratio of 2:1:1 are 0.56 and 0.25 s, respectively, which are comparatively lesser than the values reported in relevant studies [28]. The obtained fast response at the
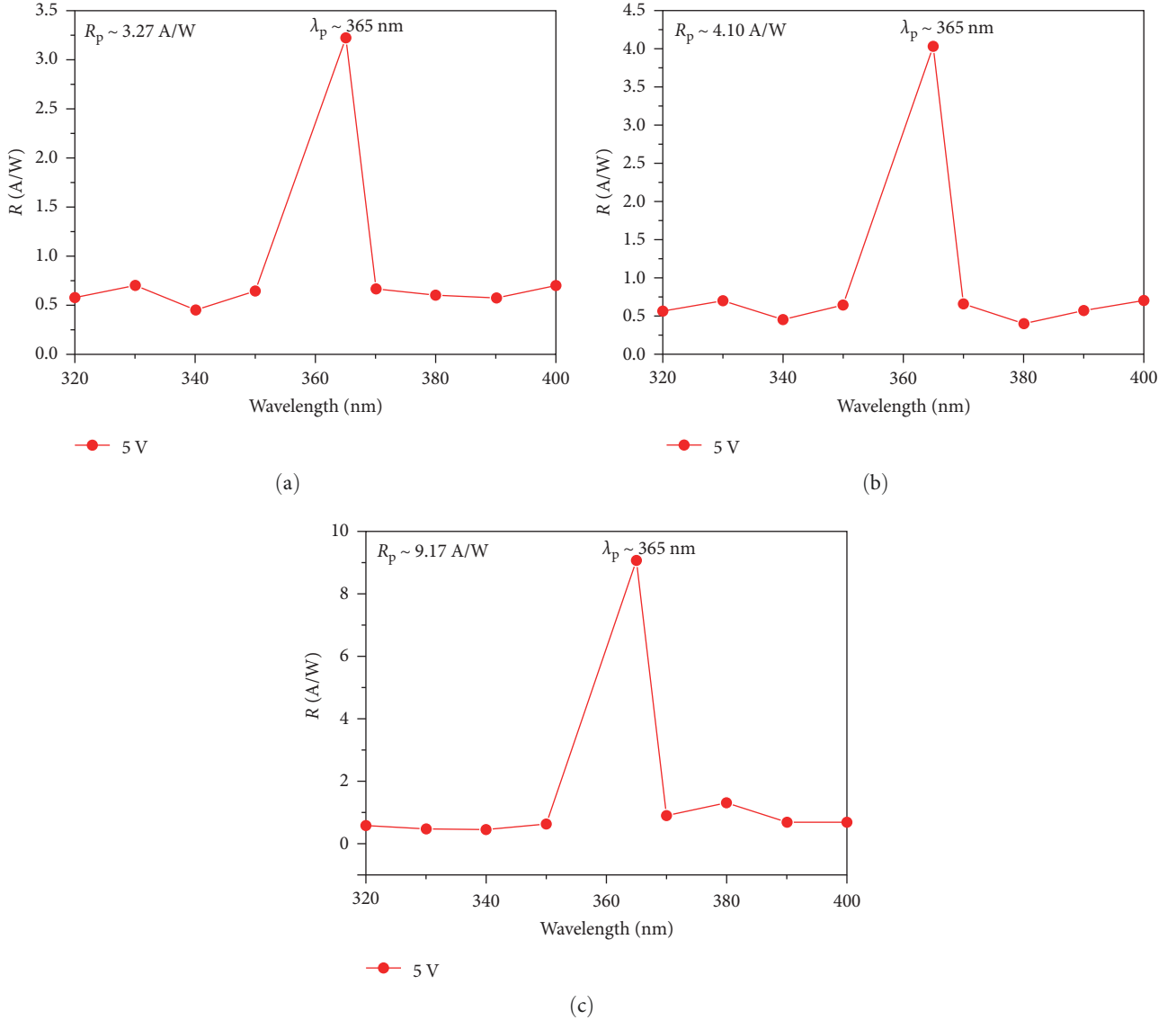
(a)

(b)

(c)

FIGURE 10: Responsivity plots of the MSM photodetector at bias voltage of +5 V for different anodization (HF:C$_2$H$_6$O:H$_2$O$_2$) chemical ratios: (a) $(1:1:0)$, (b) $(1:3:0)$, and (c) $(2:1:1)$.

optimum anodization chemical ratio $(2:1:1)$ is possibly due to the defect-free nature, high quality, and considerable photoactive surface area of the synthesized n-PSi. Therefore, it is crucial to note that the rapid response of the photodetector is typically associated with the short transit time of photo-generated carriers that have long lifetimes [14], while the gradual response duration is associated with the incidence of grain margins and increase in surface adsorption of O$_2$ [26].

The photodetection performance can be assessed based on its responsivity (R), which is can be calculated as the ratio of device photocurrent to incident optical power [29], as expressed below (Equation 8):

$$R = \frac{I_{\text{ph}}}{P_{\text{inc}}} = \frac{I_{\text{ph}}}{E.A}, \tag{8}$$

where E denotes the photon beam energy obtained by means of a conventional UV power meter (Newport power meter, Model 2936-C, USA), A is the surface area of the photodetector. The responsivity (in AW^{-1}) of the photodetector was obtained under ambient conditions in the range of 300–900 nm at a bias voltage of +5 V.

The photoresponses of the MSM photodetectors at different chemical (HF:C$_2$H$_6$O:H$_2$O$_2$) ratios are depicted in Figure 10, indicating the peak wavelength (λ_p) and peak responsivity (R_p) values. Regardless of the anodization chemical ratio, the responsivity spectra showed a distinctly observable peak at 365 nm. The R_p is highest (9.17 AW^{-1}) for the photodetector prepared at optimum anodization chemical ratio $(2:1:1)$. The apparent rise in responsivity as anodization chemical ratio is increased can be due to the specific surface area and varying thickness of the active area of n-PSi layers [14]. The maximum

TABLE 3: Parameters of the n-PSi-based photodetectors for different chemical ratios (HF:C$_2$H$_6$O:H$_2$O$_2$) and illuminated under a wavelength of 365 nm.

Anodization chemical ratio (HF:C$_2$H$_6$O:H$_2$O$_2$)	V_{Bias} (V)	I_d (A)	I_{ph} (A)	S (%)	G	R (A/W)	Φ_B (eV)	t_{Rcs} (s)	t_{Rec} (s)
(1:1:0)	3	4.43×10^{-4}	21×10^{-4}	347.04	4.47			1.68	0.89
	5	1.47×10^{-4}	10×10^{-4}	566.66	6.80	3.27	0.66	0.65	0.76
	7	1.90×10^{-4}	11×10^{-4}	748.94	5.78			0.77	0.81
(1:3:0)	3	9.64×10^{-5}	81.4×10^{-5}	744.39	8.44			0.65	0.70
	5	1.22×10^{-5}	36×10^{-5}	2,850.81	29.50	4.10	0.88	0.59	0.58
	7	1.47×10^{-5}	10×10^{-4}	566.66	6.80			0.57	1.40
(2:1:1)	3	2.21×10^{-5}	62.8×10^{-5}	2,741.62	28.41			0.55	0.53
	5	1.81×10^{-5}	109×10^{-6}	5,922.09	60.22	9.17	0.96	0.56	0.25
	7	6.12×10^{-5}	9.91×10^{-5}	61.921	1.61			0.50	0.45

response (9.17 AW^{-1}) of the photodetector is achieved for the sample with the highest layer thickness with a porosity that is seven times higher than values noted in related studies [30]. The high-intensity peak discernible at 365 nm originates from the upper Pt contacts, as previously observed for Au–Si-based devices [31]. Meanwhile, the slight shift in peak response from 365.29 to 365.45 is due to a structural change in the n-PSi layer.

The enhanced responsivity at lower wavelengths may be attributable to an increase in photocurrent. This is pertinent as increase in porosity at higher anodization current density generates a considerable number of $e^- – h^+$ pairs in the depletion region. This is anticipated since the depth of penetration reduces with wavelength, thus decreasing absorption in the Si substrate and concomitantly enhancing the depletion region. Therefore, the amount of $e^- – h^+$ pairs produced in the depletion region increases with decrease in wavelength. Additional observations reveal that the light responsivity declines abruptly at a lesser wavelength (blue and near UV), largely attributable to the absorption of photons in the n-PSi film, thus opposing its influx into the depletion region [23]. The responsivity value obtained in this study is higher compared to the value reported by Hadjersi and Gabouze [23].

The percentage quantum efficiency (η) of the photodetector is described on the basis of the amount of accumulated charge carriers required to generate the photocurrent (I_{ph}) for a specific incident optical power (P_{in}) using Equation (9):

$$\eta(\%) = \frac{I_{ph}}{q} \frac{h\nu}{P_{in}}. \qquad (9)$$

The quantum efficiency of the photodetector in terms of responsivity (R) gives the underlying Equation (10) [32]:

$$\eta(\%) = \frac{hc}{Gq\lambda} R = \frac{1.24R}{g\lambda(\mu m)}, \qquad (10)$$

where G denotes the current gain of the photodetector, while the other symbols have been explained in previous equations. The G can be derived from the ratio of accumulated electrons per unit of time in the dark to the number of absorbed photons to generate a photoelectron per unit of

time [33]. G is derived from the I–V properties using Equation (11):

$$G = \frac{I_{ph}}{I_d}. \qquad (11)$$

At 365 nm (intensity of 1.5 mW cm^{-2}) and a bias voltage of +5 V, the calculated value of G is ~60.22 (Table 3). The reversibility of the photodetector was determined through the measurement of optical response (dynamic response time) when subjected to UV illumination. Table 3 outlines the performance parameters of the photodetectors fabricated from n-PSi prepared using different HF:C$_2$H$_6$O:H$_2$O$_2$ ratios. It can be easily deduced that the photodetector fabricated from n-PSi synthesized at the optimum chemical ratio (2:1:1) exhibited the best photodetection performance.

4. Conclusion

This study showed that the intrinsic properties of n-PSi can be controlled by varying the HF:C$_2$H$_6$O:H$_2$O$_2$ chemical ratio. The HF:C$_2$H$_6$O:H$_2$O$_2$ chemical ratio was, thus, optimized at 2:1:1. The photodetector fabricated from n-PSi synthesized at optimum chemical ratio (2:1:1), using planer interdigitated electrodes, exhibited excellent photodetection performance. The detector displayed a rapid photoresponse with a rise time of 0.56 s. The obtained responsivity (R_p) value of 9.17 at 365 nm is significantly higher than values reported for TiC/porous Si/Si. The good stability and repeatability, rapid response, and recovery of the MSM UV photodetector were credited to the high porosity and defect-free feature of the n-PSi thin films.

Data Availability

All th data used have been included in this manuscript.

Additional Points

Highlights. Investigates the influence of the chemical ratio of precursor materials (HF:C$_2$H$_6$O:H$_2$O$_2$) on the structural, morphological, optical, and electric properties of PSi. The PSi was produced by photoelectrochemical etching followed

by subsequent anodization of the n-type Si under light illumination. The HF:C_2H_6O:H_2O_2 chemical ratio was optimized at 2 : 1 : 1. A MSM ultraviolet photodetector (Pt/n-PSi/Pt) was fabricated. The responsivity of the laser-annealed n-Psi with different chemical ratio can reach as high as 9.17 A/W. The current gain under 365 nm UV illumination is 60.22.

Conflicts of Interest

The authors declare that they have no conflicts of interest.

Authors' Contributions

Asad A Thahe: conceptualization, methodology, experiment, and writing-original draft preparation. M.A. Qaeed and A. Mindil: data curation and original draft co-writing. Suhail Najm Abdullah: writing-reviewing, editing, and methodology. Hasan Alqaraghuli: visualization and investigation. Ibrahim M. Badawy: validation. Yasser Saleh Mustafa Alajerami and Ammar AL-Farga: testing, conceptualization, and methodology.

Acknowledgments

References

[1] M. Drăghici, M. L. Ciurea, and V. Iancu, "The investigation of trapping levels in nanocrystalline porous silicon by optical charging spectroscopy," *Fizica Stării Condensate*, vol. 76, pp. 86–90, 2000.

[2] D. Buttard, D. Bellet, G. Dolino, and T. Baumbach, "Thin layers and multilayers of porous silicon: X-ray diffraction investigation," *Journal of Applied Physics*, vol. 83, no. 11, pp. 5814–5822, 1998.

[3] S. E. El-Zohary, M. A. Shenashen, N. K. Allam, T. Okamoto, and M. Haraguchi, "Electrical characterization of nanopolyaniline/porous silicon heterojunction at high temperatures," *Journal of Nanomaterials*, vol. 2013, Article ID 568175, 8 pages, 2013.

[4] A. A. Thahe, N. Bidin, Z. Hassan et al., "Photo-electrochemically synthesized light emitting nanoporous silicon based UV photodetector: influence of current density," *Materials Research Express*, vol. 4, no. 11, Article ID 116203, 2017.

[5] S. Basu and J. Kanungo, "Nanocrystalline porous silicon," in *Crystalline Silicon-Properties and Uses*, pp. 219–250, IntechOpen, 2011.

[6] D. Buttard, D. Bellet, and G. Dolino, "X-ray-diffraction investigation of the anodic oxidation of porous silicon," *Journal of Applied Physics*, vol. 79, no. 10, pp. 8060–8070, 1996.

[7] K. Omar, Y. Al-Douri, A. Ramizy, and Z. Hassan, "Stiffness properties of porous silicon nanowires fabricated by electrochemical and laser-induced etching," *Superlattices and Microstructures*, vol. 50, no. 2, pp. 119–127, 2011.

[8] D. C. Chang, V. Baranauskas, and I. T. Prohaska, "Observation of structural depth profiles in porous silicon by atomic force microscopy," *Journal of Porous Materials*, vol. 7, pp. 349–352, 2000.

[9] A. V. Moholkar, S. M. Pawar, K. Y. Rajpure, S. N. Almari, P. S. Patil, and C. H. Bhosale, "Solvent-dependent growth of sprayed FTO thin films with mat-like morphology," *Solar Energy Materials and Solar Cells*, vol. 92, no. 11, pp. 1439–1444, 2008.

[10] A. M. Selman and Z. Hassan, "Highly sensitive fast-response UV photodiode fabricated from rutile TiO_2 nanorod array on silicon substrate," *Sensors and Actuators A: Physical*, vol. 221, pp. 15–21, 2015.

[11] O. Bisi, S. Ossicini, and L. Pavesi, "Porous silicon: a quantum sponge structure for silicon based optoelectronics," *Surface Science Reports*, vol. 38, no. 1–3, pp. 1–126, 2000.

[12] T. P. Nguyen, P. Le Rendu, V. H. Tran, V. Parkhutik, and R. Fenollosa Esteve, "Electrical and optical properties of conducting polymer/porous silicon structures," *Journal of Porous Materials*, vol. 7, pp. 393–396, 2000.

[13] M. Nabil and H. A. Motaweh, "Enhanced thermal stability of promising nano-porous silicon powder," *Advances in Nanoparticles*, vol. 5, no. 4, pp. 199–205, 2016.

[14] A. M. Selman, Z. Hassan, M. Husham, and N. M. Ahmed, "A high-sensitivity, fast-response, rapid-recovery p-n heterojunction photodiode based on rutile TiO_2 nanorod array on p-Si(1 1 1)," *Applied Surface Science*, vol. 305, pp. 445–452, 2014.

[15] A. Ramizy, Z. Hassan, and K. Omar, "Porous silicon nanowires fabricated by electrochemical and laser-induced etching," *Journal of Materials Science: Materials in Electronics*, vol. 22, pp. 717–723, 2011.

[16] L. Hu, M. Chen, W. Shan et al., "Stacking-order-dependent optoelectronic properties of bilayer nanofilm photodetectors made from hollow ZnS and ZnO microspheres," *Advanced Materials*, vol. 24, no. 43, pp. 5872–5877, 2012.

[17] A. Borodin and M. Reichling, "Characterizing TiO_2(110) surface states by their work function," *Physical Chemistry Chemical Physics*, vol. 13, no. 34, pp. 15442–15447, 2011.

[18] P. R. Norton, J. W. Goodale, and E. B. Selkirk, "Adsorption of co on Pt(111) studied by photoemission, thermal desorption spectroscopy and high resolution dynamic measurements of work function," *Surface Science*, vol. 83, no. 1, pp. 189–227, 1979.

[19] B. E. B. Al-Jumaili, Z. A. Talib, A. Ramizy et al., "Responsivity dependent anodization current density of nanoporous silicon based MSM photodetector," *Journal of Nanomaterials*, vol. 2016, Article ID 1890364, 8 pages, 2016.

[20] X. Gu, M. Zhang, F. Meng, X. Zhang, Y. Chen, and S. Ruan, "Influences of different interdigital spacing on the performance of UV photodetectors based on ZnO nanofibers," *Applied Surface Science*, vol. 307, pp. 20–23, 2014.

[21] A. F. Abd Rahim, M. R. Hashim, and N. K. Ali, "High sensitivity of palladium on porous silicon MSM photodetector," *Physica B: Condensed Matter*, vol. 406, no. 4, pp. 1034–1037, 2011.

[22] P. Vitanov, M. Kamenova, N. Tyutyundzhiev, M. Delibasheva, E. Goranova, and M. Peneva, "High-efficiency solar cell using a thin porous silicon layer," *Thin Solid Films*, vol. 297, no. 1-2, pp. 299–303, 1997.

[23] T. Hadjersi and N. Gabouze, "Photodetectors based on porous silicon produced by Ag-assisted electroless etching," *Optical Materials*, vol. 30, no. 6, pp. 865–869, 2008.

[24] J. M. Perez, J. Villalobos, P. McNeill et al., "Direct evidence for the amorphous silicon phase in visible photoluminescent porous silicon," *Applied Physics Letters*, vol. 61, no. 5, pp. 563–565, 1992.

[25] D. Dimova-Malinovska and M. Nikolaeva, "Transport mechanisms and energy band diagram in ZnO/porous Si light-emitting diodes," *Vacuum*, vol. 69, no. 1–3, pp. 227–231, 2002.

[26] A. Chouket, B. Cherif, N. Ben Salah, and K. Khirouni, "Optical and electrical properties of porous silicon impregnated with Congo red dye," *Journal of Applied Physics*, vol. 114, no. 24, Article ID 243105, 2013.

[27] H. R. Abd, Y. Al-Douri, N. M. Ahmed, and U. Hashim, "Alternative-current electrochemical etching of uniform porous silicon for photodetector applications," *International Journal of Electrochemical Science*, vol. 8, pp. 11461–11473, 2013.

[28] N. M. Ahmed, Z. Hassan, N. Alhardan et al., "Porous silicon based violet-UV detector," *AIP Conference Proceedings*, vol. 1502, pp. 196–210, 2012.

[29] L. Guo, H. Zhang, D. Zhao et al., "High responsivity ZnO nanowires based UV detector fabricated by the dielectrophoresis method," *Sensors and Actuators B: Chemical*, vol. 166-167, pp. 12–16, 2012.

[30] M. Jo, K. J. Lee, and S. S. Yang, "Sensitivity improvement of the surface acoustic wave ultraviolet sensor based on zinc oxide nanoparticle layer with an ultrathin gold layer," *Sensors and Actuators A: Physical*, vol. 210, pp. 59–66, 2014.

[31] A. Ercan and K. Minoglou, "A model to estimate QE/MTF of thinned, back-side illuminated image sensors," *Optical and Quantum Electronics*, vol. 47, pp. 1267–1282, 2015.

[32] N. H. Al-Hardan, M. J. Abdullah, N. M. Ahmed, F. K. Yam, and A. Abdul Aziz, "UV photodetector behavior of 2D ZnO plates prepared by electrochemical deposition," *Superlattices and Microstructures*, vol. 51, no. 6, pp. 765–771, 2012.

[33] N. Naderi and M. R. Hashim, "Porous-shaped silicon carbide ultraviolet photodetectors on porous silicon substrates," *Journal of Alloys and Compounds*, vol. 552, pp. 356–362, 2013.